Solar Physics
DOI: 10.1007/•••••-•••-•••-••••-•

Characterization of the Turbulent Magnetic Integral Length in the Solar Wind: From 0.3 to 5 Astronomical Units

M.E. Ruiz[1,2] · **S. Dasso**[1,2,3] · **W.H. Matthaeus**[4] · **J.M. Weygand**[5]

© Springer ••••

Abstract

The solar wind is a structured and complex system, in which the fields vary strongly over a wide range of spatial and temporal scales. As an example, the turbulent activity in the wind affects the evolution in the heliosphere of the integral turbulent scale or correlation length [λ], usually associated with the breakpoint in the turbulent-energy spectrum that separates the inertial range from the injection range. This large variability of the fields demands a statistical description of the solar wind. In this work, we study the probability distribution function (PDF) of the magnetic autocorrelation lengths observed in the solar wind at different distances from the Sun. We use observations from *Helios*, ACE, and *Ulysses* spacecraft. We distinguish between the usual solar wind and one of its transient components (Interplanetary Coronal Mass Ejections, ICMEs), and study also solar wind samples with low and high proton beta [$\beta_{\rm p}$]. We find that in the last 3 regimes the PDF of λ is a log-normal function, consistent with the multiplicative and non-linear processes that take place in the solar wind, the initial λ (before the Alfvénic point) being larger in ICMEs.

Keywords: Magnetohydrodynamics; Turbulence; Magnetic Fields, Interplanetary; Solar Wind, Theory; Coronal Mass Ejections, Interplanetary

[1] Instituto de Astronomía y Física del Espacio (CONICET-UBA), CC 67, Suc. 28, 1428, Buenos Aires, Argentina.
email: meruiz@iafe.uba.ar email: meruiz@iafe.uba.ar
[2] Departamento de Física, Facultad de Ciencias Exactas y Naturales, UBA, Pabellón 1 (1428), Buenos Aires, Argentina.
email: dasso@df.uba.ar
[3] Departamento de Ciencias de la Atmósfera y los Océanos, Facultad de Ciencias Exactas y Naturales, UBA, Pabellón 2 (1428), Buenos Aires, Argentina.
email: sdasso@at.fcen.uba.ar
[4] Bartol Research Institute, Department of Physics and Astronomy, University of Delaware, Newark, DE, USA.
[5] Institute of Geophysics and Planetary Physics, University of California, Los Angeles, CA, USA.

arXiv:1404.2826v1 [physics.space-ph] 10 Apr 2014

1. Introduction

The solar wind (SW) is a very complex and structured system, where the fields are highly variable over different temporal and spatial scales. However, despite its complexity, different types of phenomena generally associated with different scales in the SW can be identified.

At the global scale, the SW steady expansion has direct consequences on the typical length scales at which the bulk physical quantities that characterize the state of the system vary (*e.g.*, mass density, magnetic-field components, temperature). Between 0.3 astronomical unit (AU) and 5 AU from the Sun, these quantities typically decay as a power law with a negative exponent of the order of one to three (Mariani and Neubauer, 1990). Then, at a distance D from the Sun, the "steady expansion" typical length scale can be estimated as $\approx D$.

Furthermore, different transient phenomena with origin at the solar surface produce disturbances to the steady SW. An example of these SW "transient structures" is the phenomenon of fast transient streams of plasma from coronal holes (Altschuler, Trotter, and Orrall, 1972) or interplanetary coronal mass ejections (ICMEs), which have a magnetic topology radically different from the steady SW (*e.g.*, Dasso *et al.*, 2005b). These composite structures (which can contain several smaller sub-structures such as shock waves, plasma sheaths, *etc.*) are meso-scale objects in the system, with a range of sizes that are some fraction of D.

In SW turbulence, the largest spatial scale of the inertial range can be approximated by the turbulent integral scale $[\lambda]$ (see Equation (3) for a proper definition), which is also a proxy for the typical size of the "energy-containing eddies" (*e.g.*, Matthaeus *et al.*, 1994). The inertial range extends from λ to much smaller scales, involving turbulent processes along several orders of magnitude. It is very rich in non-linear processes (see for example Coleman, 1968), combined with an important level of wave activity (see for example Belcher and Davis, 1971). This complex turbulent activity affects the evolution of different aspects of the SW fluctuations, such as the fluctuating intensity, the integral length $[\lambda]$, the level of Alfvénicity (Tu and Marsch, 1995), anisotropy (Matthaeus, Goldstein, and Roberts, 1990; Dasso *et al.*, 2005a; Ruiz *et al.*, 2011), *etc.* In particular, it is well known that λ increases with heliocentric distance (Tu and Marsch, 1995). Near Earth λ_{1AU} is ≈ 0.0079 AU (Matthaeus *et al.*, 2005) while λ_{10AU} is ≈ 0.046 AU in the SW near Saturn (Smith *et al.*, 2001).

All of these physical phenomena, associated with significantly different spatial scales, are coupled. For instance: i) the decay of the total solar-wind pressure (determined by its "steady expansion" scale) plays the major role during the long-term interaction between magnetic clouds and their environment (Démoulin and Dasso, 2009; Gulisano *et al.*, 2010; Gulisano *et al.*, 2012), ii) the presence of shear in the velocity profile (*e.g.*, associated with CIRs or ICMEs) can produce instabilities and introduce energy into the outer scales of the turbulent inertial range (Goldstein, Roberts, and Matthaeus, 1995), iii) turbulent properties control the drag on ICMEs and many other large-scale processes (Matthaeus and Velli, 2011), *etc.*

An important entity for studying fluctuations of turbulent fields is the autocorrelation function. For the magnetic field, the average trace of the two-point/two-time correlation tensor is

$$R([\boldsymbol{x},t],[\boldsymbol{r},\tau]) = \langle \boldsymbol{b}(\boldsymbol{x},t)\cdot\boldsymbol{b}(\boldsymbol{x}+\boldsymbol{r},t+\tau)\rangle \tag{1}$$

where $\boldsymbol{b}$ is the fluctuating component of $\boldsymbol{B}$ and $[\boldsymbol{r},\tau]$ are the spatial and temporal lags, respectively. We can drop the $[\boldsymbol{x},t]$ dependence in Equation (1) if we assume stationarity and homogeneity of the medium (Matthaeus and Goldstein, 1982; Bruno and Carbone, 2013). Further, we may assume the Taylor frozen-in-flow hypothesis (Taylor, 1938) to be valid in the supersonic and super-Alfvénic SW; that is, the fluctuating fields are convected past the spacecraft in a shorter time than their characteristic dynamical timescale. Then we can ignore the intrinsic temporal dependence of the fluctuations in Equation (1), resulting in

$$R(\boldsymbol{r}) = \langle \boldsymbol{b}(\mathbf{o})\cdot\boldsymbol{b}(\boldsymbol{r})\rangle \tag{2}$$

The spatial decorrelation of the turbulence can be characterized by the correlation length or integral scale

$$\lambda = \frac{\int_0^\infty \langle\, \boldsymbol{b}(\mathbf{o})\cdot\boldsymbol{b}(\boldsymbol{r})\,\rangle}{\langle \boldsymbol{b}^2\rangle \mathrm{d}r} \tag{3}$$

Conventionally, this typical length-scale is understood as being a measure of the size of the turbulent energy-containing eddies in the flow (Batchelor, 1953). Moreover, λ can be linked to the scale associated with the spectral break that separates the injection range (meso-scales) from the inertial range: λ can be seen as a kind of spatial frontier between the two domains.

Any description of the complex SW physical system should be complemented by a statistical description of the fields, since important information about turbulent systems resides at a statistical level and, to this day, it is not possible to measure initial or boundary conditions (Burlaga and Lazarus, 2000).

Log-normal distributions are frequent in nature across the different branches of science (Limpert, Stahel, and Abbt, 2001), and are believed to be a consequence of multiplicative processes (*e.g.*, Montroll and Shlesinger, 1982). In particular, in the field of space and solar physics, many authors have considered log-normal distributions when modelling quantities of interest such as the Dst index (Campbell, 1996), the magnitude of the magnetic field fluctuations (Burlaga and Ness, 1998; Padhye, Smith, and Matthaeus, 2001), SW speed, proton density and temperature (Burlaga and Lazarus, 2000), proton plasma beta and Alfvén speed (Mullan and Smith, 2006).

As far as we know, the probability distribution functions (PDFs) of autocorrelation lengths [λ] of the solar-wind fluctuating magnetic field have not been studied. Wicks, Owens, and Horbury (2010) reported an asymmetric shape for the observed PDF of the correlation lengths of the magnetic field magnitude at 1 AU. Matthaeus and Goldstein (1986) had theoretically postulated that λ is log-normally distributed. The authors explained that the structures that initiate the cascade in the inertial range, amplify their initial size λ_0 during their transport

into the SW from the solar surface, employing a mechanism of successive magnetic reconnection events to increase the size of magnetic structures. This occurs M times each one by a factor $(1+\epsilon)$ yielding a final size given by $\lambda = \lambda_0(1+\epsilon)^M$ with λ the correlation length of the fluctuations. If M is sufficiently large, the random variable $\ln(\lambda)$ will be normally distributed and therefore λ log-normally distributed.

Thus, the discussion presented in this Section motivates us to study λ in the SW and its evolution. One of the main aims of this article is to provide an observational characterization of the PDF of λ.

2. Data and Procedure

We use the magnetic field and plasma observations collected by different spacecraft that repeatedly explored the inner and outer heliosphere at different heliocentric distances D. In particular we analysed *in-situ* solar wind observations from the following four probes: *Helios* 1 (H1), *Helios* 2 (H2), Advanced Composition Explorer (ACE), and *Ulysses*. Our H1 and H2 time series cover the period from December 1974 to June 1981, the temporal cadence is 40 seconds and observations are essentially on the Ecliptic plane. Near-Earth observations coming from the ACE spacecraft cover the period from February 1998 to March 2008, with time cadence of one minute. *Ulysses* series range from November 1990 to May 2009, and the temporal cadence is of one minute. We restrict our *Ulysses* observations to the Ecliptic plane by choosing heliocentric latitudes $[\theta]$ such that $|\theta| < 30^\circ$.

For each spacecraft (labeled s) we group the data into 24-hour-length intervals $[I]$, thus obtaining N_1^s subseries (intervals). Due to the presence of many gaps in the *Helios* data, we repeat the procedure for H1 and H2 only by shifting the data by 12 hours to obtain $N_2^{s=H1,H2}$ additional intervals, thus maximizing *Helios* data utilization.

We avoid samples with very low statistical significance by retaining only those intervals encompassing at least the 30 % of the observations expected for the cadence mentioned for each spacecraft.

We compute the magnetic correlation functions and respective correlation lengths as follows: in each interval $[I]$ and for each spacecraft $[s]$, from the observed magnetic field time series $[\mathbf{B}^{I,s}]$ we construct the magnetic fluctuations as $\mathbf{b}^{I,s} = \mathbf{B}^{I,s} - \mathbf{B}_0^{I,s}$, with $\mathbf{B}_0^{I,s}$ a linear fit to $\mathbf{B}^{I,s}$ data. Here we identify the fitted field $[\mathbf{B}_0^{I,s}]$ with the local (within the interval) estimate of the average magnetic field in an ensemble.

Next, we compute each correlation function $[R^{I,s}]$ using the Blackman–Tukey technique, in the same way as was done in Milano *et al.* (2004). Inside the Alfvénic point, the different initial conditions will yield different initial values for $R(\mathbf{0}) = \langle b^2 \rangle$ and for λ. So, in order to be able to compare intervals with different fluctuating amplitude, we normalize the correlation functions as $R^{I,s}_{norm} = R^{I,s}/R(\mathbf{0})^{I,s}$. For simplicity of notation, we drop the labels *norm* and s hereafter.

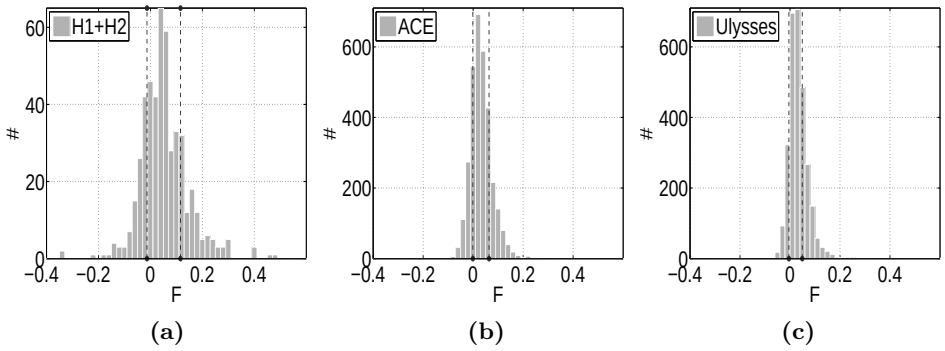

Figure 1. Histograms of the quality factor index [F]. Dashed vertical lines indicate the position of the 20^{th} (left) and 80^{th} (right) percentile. Panels (a), (b), and (c) correspond to H1+H2, ACE and *Ulysses* data respectively.

Figure 1 in Ruiz *et al.* (2011) shows a typical correlation function in the inner heliosphere that can be obtained with the Blackman–Tukey technique. Correlation functions in the outer heliosphere have a similar shape.

A simple approximation that is often used to the shape of R^I, at large scales and in the long wavelength part of the inertial range, is an exponential decay $R \approx \exp(-r/\lambda)$. This approximation provides us with two methods, i) and ii), to estimate the magnetic autocorrelation length λ^I in each interval. The first method determines an estimate of λ_i^I as the value of the spatial lag such that the decreasing function R^I reaches $\exp(-1)$ for the first time, *i.e.*, $R^I(\lambda_i^I) = 1/e$. Method ii) consists in parametrizing the correlation function as $\ln(R) \approx -r/\lambda$. We estimate λ_{ii}^I as minus the inverse of the slope obtained from a linear fit to $\ln(R)$ vs. r.

It is accepted that for steady turbulence, magnetic autocorrelation functions behave as shown in Figure 1 in Ruiz *et al.* (2011). Departures from this shape can imply the presence of transient events (*e.g.*, large-scale current-sheet crossings).

Under the approximation $R \approx \exp(-r/\lambda)$ for the autocorrelation functions, we find that steady turbulent intervals are characterized by $\lambda_i^I \simeq \lambda_{ii}^I$, while intervals far away from steady turbulence show values of λ_{ii}^I very different to λ_i^I. This fact allows us to define a quality factor F of the correlation function, based on the two estimates of the correlation length. We define this factor as

$$F^{s,I} = \frac{\lambda_{ii}^{s,I} - \lambda_i^{s,I}}{\lambda_{ii}^{s,I} + \lambda_i^{s,I}} \tag{4}$$

Note that a small positive offset in F is expected due to the systematic differences in method i) and ii) (see Ruiz *et al.* (2011)). Figure 1 shows the distribution of the quality factor index [F] for the three missions analyzed in this article. We select the best intervals based on the value of F in each case, by retaining only those that fulfilled the following two conditions: F values within the interval larger than the value of the 20^{th} percentile and those with F values smaller than the value of the 80^{th} percentile. These intervals are the ones between the two

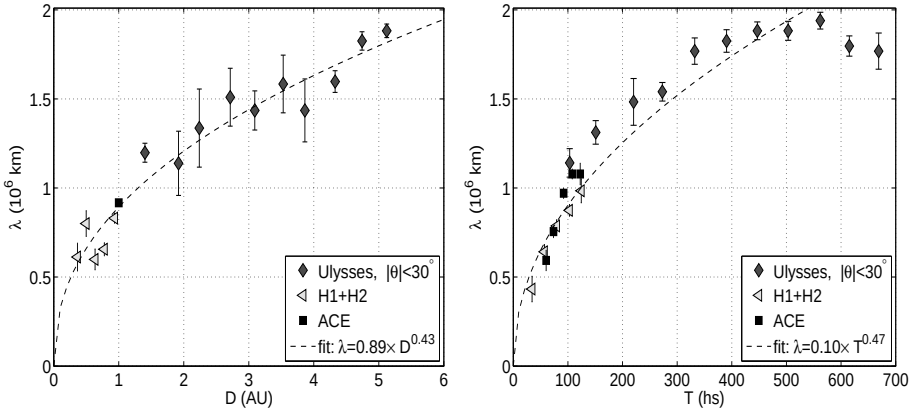

Figure 2. Observed λ vs. heliocentric distance [D] (left panel) and versus the solar-wind age (right panel). Bars show the error of the mean.

dashed vertical lines in Figure 1. Different ranges for F were explored, arriving at qualitatively similar results. The main effect of modifying the F ranges is to vary the intervals considered for each spacecraft.

Finally, after the different selection criteria, our collection of usable data includes $N_1^{s=U}$ =1976 for *Ulysses*, $N_1^{s=A}$ =1919 for ACE, and $N_1^{s=H1+H2}$ + $N_2^{s=H1+H2}$ =846 for *Helios*, where $s = H1+H2$ indicates that we have gathered H1 and H2 intervals into only one data set representative of the inner heliosphere.

3. Evolution of λ with Heliocentric Distance and Nominal Aging

Turbulent structures evolve and are advected by the solar wind throughout the heliosphere with the SW velocity [$V_{\rm sw}$]. A key quantity for closing MHD turbulence models is the similarity scale, usually identified with the correlation scale for the fluctuations. Observational insight into the evolution of correlation lengths is useful when comparing with numerical solutions or choosing proper boundary conditions.

The left panel of Figure 2 shows how the observed λ by *Helios* (triangles), ACE (squares), and *Ulysses* (diamonds) evolves with heliocentric distance. The observations have been grouped into bins of different width (ΔD =0.14 AU for H1+H2 data and ΔD =0.4 AU for *Ulysses* data), and each value of the vertical axis is the median of λ within the bin.

λ increases with heliocentric distance both in the inner and outer heliosphere, as has been shown in previous observational works (*e.g.*, Matthaeus, Smith, and Bieber, 1999; Bruno *et al.*, 2005; Bruno *et al.*, 2009; D'Amicis *et al.*, 2010) and model calculations (*e.g.*, Smith *et al.*, 2001). A least-squares fit to the data (dashed line), illustrates this behavior, yielding a power law $\lambda(D) = 0.89(D/1\,AU)^{0.43} \times 10^6$ km. Other exponents for the power laws have been reported (*e.g.*, Klein *et al.*, 1992). Moreover, between 1 AU and 5 AU, the growth rate of λ with heliocentric distance is $\Delta\lambda/\Delta D \approx 0.0015$, very close to

the predictions of the model of Smith *et al.* (2001) with the strongest shear as the driver of the turbulence. On the contrary, observations reported by D'Amicis *et al.* (2010), show a larger growth rate between 1 AU and 1.4 AU, $\Delta\lambda/\Delta D \approx 0.063$ than observations reported here ($\Delta\lambda/\Delta D \approx 0.0023$). Nevertheless, while they observed fast (Alfvénic) solar wind, we observed mixed fast and slow wind. Shear intensity is typically higher in slow than fast solar wind (McComas *et al.*, 2003), and the more intense the shear is, the more slowly correlation lengths increase. On the Ecliptic plane, the slow wind is more frequently encountered than the fast wind, so that slow SW properties are favored when computing averages. Other authors have studied the evolution of turbulent fluctuations in fast polar wind (*e.g.*, Bavassano *et al.*, 1982; Horbury *et al.*, 1995; Horbury *et al.*, 1996). These authors showed that the breakpoint wavenumber in high latitude flows is smaller than that one in low latitude flows at similar heliocentric distances, revealing that polar fluctuations are less evolved than ecliptic fluctuations. Finally, this growth of λ is consistent with the shift towards low frequencies of the spectral break (this concept that was first introduced by Tu, Pu, and Wei, 1984) which separates the inertial range from the large-scale injection range, revealing that non-linear interactions at large heliocentric distances are still taking place.

While traveling throughout the heliosphere, turbulent structures will reach a spacecraft located at D after a time $\approx D/V_{\rm sw}$. For each analyzed interval $[I]$, we compute what we call the "age" of the interval I: $T^I = D^I/V^I_{\rm sw}$. Then T^I corresponds to the nominal time it takes a solar wind parcel $[I]$ moving at speed $V^I_{\rm sw}$ to travel a given distance from the Sun to the spacecraft located at D^I.

The right panel of Figure 2 shows the evolution of λ with T. The observations have been grouped into T-bins of different width (ΔT =25 hours for H1+H2 data, ΔT =18 hours for ACE and ΔT =58 hours for *Ulysses* data), and each value of the vertical axis is the median of λ within the bin.

Correlation lengths steadily grow with age until around $\approx$ 500 hours, but then they seem to decrease. A least-squares fit to the data (dashed line) yields a power law $\lambda(T) = 0.10(T/1\,\text{hour})^{0.47} \times 10^6\,\text{km}$. This globally increasing trend is consistent with numerical simulations derived from models for MHD turbulence based on the Kármán and Howarth HD approach (Oughton, Dmitruk, and Matthaeus, 2006).

4. Characterization of the PDF of λ

In this Section we characterize the distribution of correlation lengths of the solar wind magnetic fluctuations on the Ecliptic plane at three different distances from the Sun (*i.e.* three different stations). To allow a clear distinction between the three data sets (*i.e.* between stations), we limit *Helios* observations to heliocentric distances between 0.3 AU and 0.7 AU, and *Ulysses* observations to heliocentric distances between 3 AU and 5.3 AU.

Figure 3 presents the observed histograms of λ at each station. Heliocentric distance increases from left to right: panels *a*, *b*, and *c* corresponding to H1+H2, ACE, and *Ulysses* data, respectively. As the heliocentric distance increases, the bins at the right become progressively occupied. In each case, the distribution is

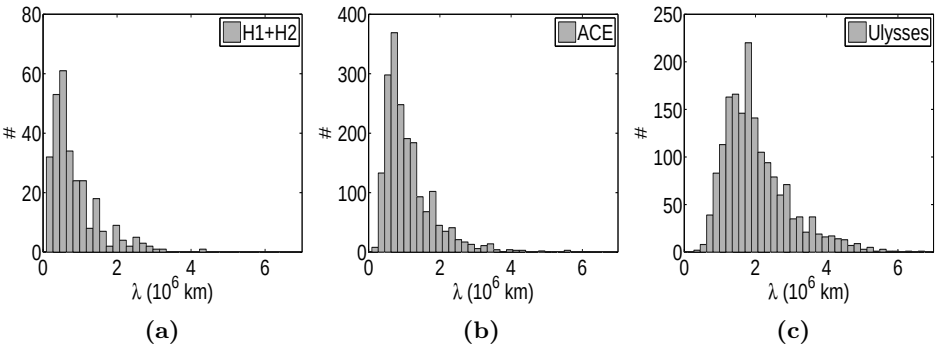

Figure 3. Observed histograms of λ. Panels (a), (b), and (c) corresponding to H1+H2, ACE, and *Ulysses* data respectively.

clearly asymmetric with a long tail on the right side. This long tail is evidence of non-linear interactions and multiplicative processes, and motivates us to explore the hypothesis of a log-normal PDF for λ.

Since normal and log-normal distributions are related (see Appendix A), we perform a statistical analysis on $\ln(\lambda)$ by computing the different moments of the histogram of $\ln(\lambda)$, and then make use of Equations (8) (Appendix A) for the statistics of λ.

Moments of higher order than the variance will become of interest since we want to study how the distribution of $\ln(\lambda)$ deviates from Gaussianity. The third, fourth, and sixth central moments of a probability distribution function are defined as follows

$$\gamma = \frac{E[(x-\mu)^3]}{\sigma^3}, \qquad K = \frac{E[(x-\mu)^4]}{\sigma^4}, \qquad M_6 = \frac{E[(x-\mu)^6]}{\sigma^6} \tag{5}$$

where E means expectation value, x a random variable, μ its expectation value, and σ its standard deviation. All odd central moments for a symmetric distribution are zero. Then any non-vanishing odd central moment can be taken as a measure of asymmetry of the distribution. Positive values of the skewness $[\gamma]$ indicate that the distribution has a larger tail to the right of the mean value, while negative values indicate a larger tail to the left. The moments K and M_6 are useful to compare with the Gaussian distribution, for which $K = 3$ and $M_6 = 15$. Any distribution with a K larger (smaller) than 3 will be higher (lower) than a Gaussian distribution with the same mean and variance. The information on how the tails of the distribution fall is contained in M_6. Values of M_6 higher than 15 indicate more slowly decreasing tails and lower values more rapidly decreasing tails than a Gaussian distribution.

Figure 4 presents the histograms of $\ln(\lambda)$, together with a non-linear least-squares fit to the data of a Gaussian trial function. There are empty bins at the left of the histogram in panel (a). This is due to the interval selection procedure followed in the present work. The definition of the quality factor $[F]$ depends explicitly on λ_{ii} calculated through a linear fit to $\ln(R) \approx -r/\lambda$. Due to the

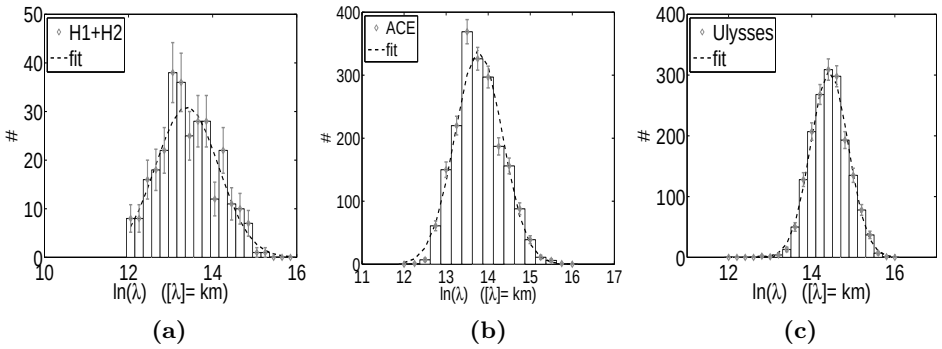

Figure 4. Histograms of $\ln(\lambda)$ and non-linear least-square fit. Panels (a), (b), and (c) correspond to H1+H2, ACE, and *Ulysses* data respectively.

time cadence available, for correlation functions decreasing very fast it is not possible to fit a straight line since there is only one point available in the region of interest. These cases, which fill the bins to the left, were assigned with a flag and were excluded from the analysis.

Table 1 shows the relevant statistical parameters of the distributions of λ (see Figure 3) and $\ln(\lambda)$ (see Figure 4).

The first panel presents the moments of the observed $\ln(\lambda)$ distribution, obtained directly from the data: mean $[\mu]$ and variance $[\sigma^2]$, skewness $[\gamma]$, kurtosis $[K]$ and sixth central moment $[M_6]$. We included the mean value $[m]$ and median $[m^*]$ of the λ distribution (Figure 3) obtained from Equations (8).

The second panel presents the values of the parameters returned by the non-linear least-square fits to the data: mean $[\mu]$ and variance $[\sigma^2]$, number of degrees of freedom $[dof]$, minimum $[\chi^2]$, and mean $[m]$ and median $[m^*]$ of the λ distribution. A comparison between the moments obtained from data and those obtained through the fits is shown in the third panel, where we report the ratios between panel 1 (P1) and panel 2 (P2) quantities. As expected, values obtained directly from data and values obtained from the fitting procedure are remarkably similar.

The number of intervals $[I]$ considered in each case are shown in the last row of Table 1.

As D increases, moments (from observations and from fits) evolve to have the same values (panel 3 of Table 1), the fourth and sixth central moments show a trend to reach the values expected for a Gaussian distribution, and the variance decreases. The skewness does not show a definite trend, but nevertheless it does not depart too much from the zero expected for a symmetric distribution.

5. Hypothesis Testing

Histograms and the different moments of the observed $\ln(\lambda)$ distribution are useful for the characterization of the asymptotic PDF and, although they may quantify deviations from Gaussianity, they are not enough to give conclusive

Table 1. Statistical parameters of $\ln(\lambda[\mathrm{km}])$ distributions shown in Figure 4. First panel: values from the observed PDF. Second panel: values from the non-linear least-squares fit. Third panel is a comparison between the first two. We also show in panel 4 the Pv from KS goodness-of-fit test. The number of intervals analyzed in each case is reported in the last row.

Panel 1: From observations			
	H1+H2	ACE	*Ulysses*
μ	13.42	13.78	14.43
σ^2	0.47	0.30	0.19
γ	0.21	0.35	0.04
K	2.49	2.79	2.94
M_6	9.75	12.40	12.71
m ($\times 10^6$ km)	0.85	1.12	2.03
m^*($\times 10^6$ km)	0.67	0.97	1.85
Panel 2: From non-linear fit to data			
	H1+H2	ACE	*Ulysses*
μ	13.39	13.78	14.43
σ^2	0.56	0.32	0.20
m ($\times 10^6$ km)	0.86	1.13	2.04
m^*($\times 10^6$ km)	0.65	0.96	1.84
dof	18	15	19
χ^2	17.70	60.19	23.5
Panel 3: Comparing panel 1 with panel 2			
	H1+H2	ACE	*Ulysses*
μ_{P1}/μ_{P2}	1.002	1	1
$\sigma^2_{P1}/\sigma^2_{P2}$	0.84	0.94	0.95
m_{P1}/m_{P2}	0.99	0.99	0.995
m^*_{P1}/m^*_{P2}	1.03	1.01	1.01
Panel 4: JB goodness-of-fit test			
	H1+H2	ACE	*Ulysses*
Pv	0.06	$<$0.01	0.71
# of intervals	291	1919	1731

evidence that the model, log-normal PDF of λ, is appropriate or not. We employ then a more formal method, the Jarque–Bera (JB) goodness-of-fit hypothesis test (Jarque and Bera, 1980; Thadewald and Büning, 2007) to support and complement the graphical methods presented above in Section 4.

The JB test is useful to check the normality assumption, that is, to test the hypothesis H_0 that the random variable $\ln(\lambda)$ is drawn from a normal distribution function with unknown mean and unknown variance, against an alternative

hypothesis that $\ln(\lambda)$ does not come from a normal distribution. This test is suitable when the hypothesized distribution is not known and its parameters (mean and variance) have to be estimated.

The test statistic [ξ_{JB}] is defined as

$$\xi_{JB} = \frac{n}{6}\left(\gamma^2 + \frac{(K-3)^2}{4}\right) \tag{6}$$

where n is the number of data points, γ is the sample skewness, and K is the sample kurtosis; ξ_{JB} is asymptotically χ^2 distributed with two degrees of freedom (Jarque and Bera, 1980). Here we want to emphasize that, for the normal distribution the skewness and kurtosis are quantities with defined values.

We then, at each spatial station independently, implement the JB test on $\ln(\lambda)$, proposing that its PDF is Gaussian. We use the built-in MatLab function and test the hypothesis at a (conventional) 0.05 significance level [α] (e.g., Frodesen, Skjeggestad, and Tofte, 1979). Results are presented in the fourth panel of Table 1 in terms of the P-value [Pv] (the largest α that can be tolerated without rejecting H_0): values of Pv larger than α indicate to accept the H_0, otherwise H_0 should be rejected (see Appendix B).

The values of Pv obtained for H1+H2 and *Ulysses* data sets, Pv =0.06 and Pv =0.71 respectively, are strong evidence supporting the hypothesis thus we may accept that magnetic autocorrelation lengths have a log-normal distribution at a 0.06 and 0.71 significance level for H1+H2 and *Ulysses* respectively.

To understand this better, suppose that we again measure correlation lengths in the inner heliosphere and we present the data in a histogram. With this hypothesis being true, the probability of getting a histogram of $\ln(\lambda)$ such as, or worse than, the one presented here (Figure 4(a)) is given by Pv, that is a probability of 6 %. For the outer heliosphere, the result is even better, since the probability of obtaining a histogram like, or worse than, the one in Figure 4(c) is higher, meaning that the one reported here is one of the best.

Regarding ACE data, although results are qualitatively good, quantitative evidence, stated through Pv, is not sufficient to conclude that the λ-distribution is log-normal. We revisit this issue in the next Section.

6. Low and High Proton β_p

In the last section the data employed in the analysis was selected for latitude and data quality, but not selected according to values of plasma parameters. Here we include an analysis based on a familiar parameter, the proton beta [β_p]. In the SW dynamics, high or low values of β_p (proton kinetic pressure/magnetic pressure) indicate the dominant role of the gas or the magnetic field, respectively.

In low and high β_p regimes different wave modes can be triggered. There are also relations between β_p and, for example, temperature anisotropy which introduce constraints to the system and determine the properties of the instabilities in space plasma conditions (*e.g.*, Bale *et al.*, 2009). Thus, β_p is a parameter that play a key role in the regulation of waves propagation and the triggering of instabilities in the SW.

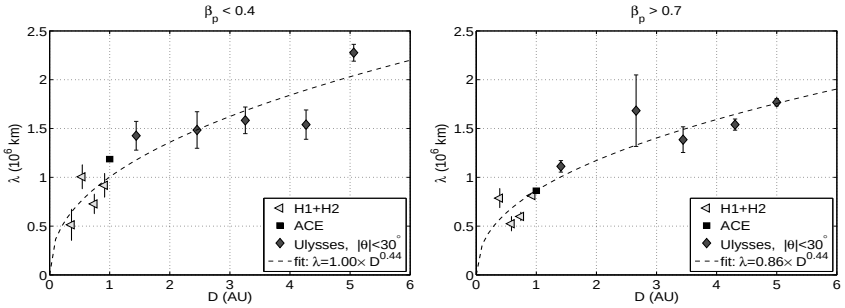

Figure 5. Plot of observed λ versus heliocentric distance for low-$\beta_{\rm p}$ and high-$\beta_{\rm p}$ regimes.

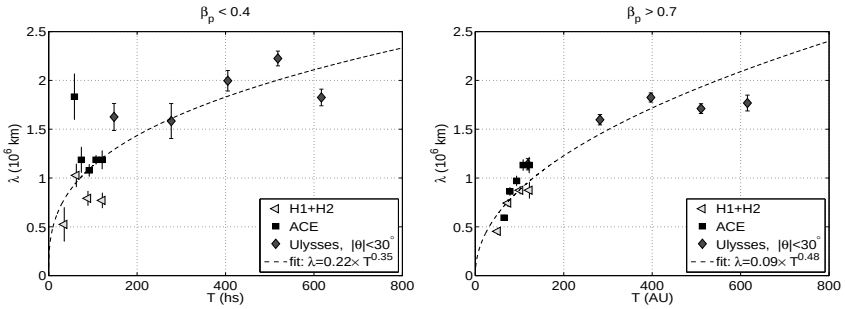

Figure 6. Plot of observed λ versus solar-wind age for low-$\beta_{\rm p}$ and high-$\beta_{\rm p}$ regimes.

In this section then we further investigate the statistics of correlation lengths when subdividing the sample into two groups with high and low values of $\beta_{\rm p}$.

As limiting $\beta_{\rm p}$ values we choose $\beta_{\rm p} = 0.4$ to define a low-$\beta_{\rm p}$ regime, and $\beta_{\rm p} = 0.7$ for the high-$\beta_{\rm p}$ regime, in order to allow a clear division between the sets while keeping a statistically significant amount of data.

Figures 5 and 6 show how correlation lengths grow with heliocentric distance and age in both regimes: $\beta_{\rm p} < 0.4$ and $\beta_{\rm p} > 0.7$. We group the observations into bins of heliocentric distance of different widths: $\Delta D = 0.17$ AU for H1+H2 data and $\Delta D = 0.85$ AU for *Ulysses* data; and into bins in turbulence age of widths $\Delta T = 28$ hours, 16 hours, 125 hours for H1+H2, ACE, and *Ulysses* respectively. A least-squares fit to the data yields a power-law increase in each case; see inset in Figures 5 and 6. It seems that observations of λ are better ordered for $\beta_{\rm p} > 0.7$ and with T.

In Figure 7 we present the non-linear least-square fit to the distributions of $\ln(\lambda)$ for the low-$\beta_{\rm p}$ and high-$\beta_{\rm p}$ groups together. Here, each of the Gaussian fits is normalized by the total area, and therefore the value of the ordinate represents a probability density. Again, heliocentric distance increases from left to right, each panel corresponding to H1+H2, ACE, and *Ulysses* observations respectively. The $\ln(\lambda)$ distribution for the low-$\beta_{\rm p}$ plasma is wider and is displaced to the

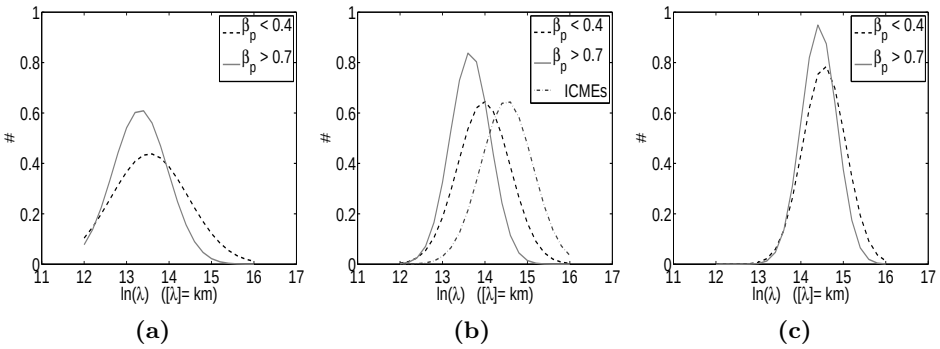

Figure 7. Non-linear least-square fit for high-β (solid line) and low-β (dashed line) samples. Panels (a), (b) and (c) correspond to H1+H2, ACE and *Ulysses* data respectively. The dashdot line in panel (b) corresponds to the non-linear least-square fit for ICMEs (see Section 7).

right when compared to the high-$\beta_{\rm p}$ plasma samples. Table 2 shows the relevant statistical parameters of the distributions shown in Figure 7. It has the same structure as Table 1: the first panel presents the moments directly obtained from the data while the fitting parameters are listed in the second panel. The third panel compares results reported in panel 1 and panel 2.

For both regimes, we again find that correlation lengths grow with increasing heliocentric distance. Moreover, we find that both populations grow approximately at the same rate, with the mean correlation length in the low-$\beta_{\rm p}$ plasma being 1.5 times higher than the mean λ in high-$\beta_{\rm p}$ plasma at *Helios* heliocentric distances, and diminishing to a ratio of 1.2 in the outer heliosphere.

We also perform a JB test on the three low-$\beta_{\rm p}$ and three high-$\beta_{\rm p}$ groups of correlation lengths to test if, when separating the observations into these two regimes, the distributions of λ are consistent with a log-normal distribution. The test is performed on the $\ln(\lambda)$ distributions, and the Pv values obtained are listed in the fourth panel of Table 2. The values of Pv, 0.06, 0.06 and 0.10 in the low-β regime, and 0.14, 0.08, 0.36 in the high-$\beta_{\rm p}$ regime for H1+H2, ACE, and *Ulysses* respectively (all of them larger than α), indicate that the hypothesis "correlation lengths are log-normally distributed in low-$\beta_{\rm p}$ SW and in high-$\beta_{\rm p}$ SW" can be accepted in all six cases at the respective Pv significance. Note that the results for ACE are greatly improved relative to the last Section which did not sort the data by $\beta_{\rm p}$. Here we see that low-β_p and high-β_p populations observed by ACE spacecraft are slightly separated, more than for *Helios* and *Ulysses* data, being the JB test is sensitive to this separation.

7. Interplanetary Coronal Mass Ejections

A typical example in the SW of low β_p are magnetic clouds (MCs), transient regions observed having a smooth rotation of the magnetic-field direction, a magnetic field strength higher than average SW, low proton temperature and thus, low $\beta_{\rm p}$ compared to the ambient SW. Typical values for $\beta_{\rm p}$ at 1 AU for ambient

Table 2. Characterization of λ distribution for low-β_p, high-β_p regimes and ICMEs observed only by ACE

Panel 1: From observations							
	β_p <0.4			β_p >0.7			ICMEs
	H1+H2	ACE	*Ulysses*	H1+H2	ACE	*Ulysses*	ACE
μ	13.57	13.98	14.55	13.35	13.68	14.42	14.52
σ^2	0.61	0.35	0.24	0.32	0.20	0.17	0.53
γ	0.13	0.07	-0.17	0.41	0.18	0.10	-0.16
K	1.96	2.58	2.65	2.61	2.62	3.11	3.08
M_6	4.88	10.10	11.57	8.88	10.33	15.27	14.00
m ($\times 10^6$ km)	1.06	1.40	2.35	0.74	0.97	1.99	2.33
m^* ($\times 10^6$ km)	0.78	1.18	2.08	0.63	0.87	1.83	2.03
Panel 2: From non-linear fit to data							
	β_p <0.4			β_p >0.7			ICMEs
	H1+H2	ACE	*Ulysses*	H1+H2	ACE	*Ulysses*	ACE
μ	13.54	13.97	14.55	13.32	13.65	14.43	14.50
σ^2	0.83	0.38	0.26	0.42	0.22	0.18	0.59
m ($\times 10^6$ km)	1.15	1.41	2.37	0.75	0.95	2.02	2.36
m^* ($\times 10^6$ km)	0.78	1.17	2.08	0.61	0.85	1.85	1.98
dof	19	19	19	19	19	19	17
χ^2	18	24	17.6	19	19	20.6	21
Panel 3: Comparison between panel 1 (P1) and panel 2 (P2)							
	β_p <0.4			β_p >0.7			ICMEs
	H1+H2	ACE	*Ulysses*	H1+H2	ACE	*Ulysses*	ACE
μ_{P1}/μ_{P2}	1.002	1.001	1	1.002	1.002	0.999	1.00
$\sigma^2_{P1}/\sigma^2_{P2}$	0.73	0.92	0.92	0.76	0.91	0.94	0.90
m_{P1}/m_{P2}	0.923	0.99	0.99	0.99	1.02	0.99	0.99
m^*_{P1}/m^*_{P2}	1	1.01	1	1.03	1.02	0.99	1.03
Panel 4: JB goodness-of-fit test							
	β_p <0.4			β_p >0.7			ICMEs
	H1+H2	ACE	*Ulysses*	H1+H2	ACE	*Ulysses*	ACE
Pv	0.06	0.06	0.10	0.14	0.08	0.36	0.29
# of intervals	101	675	409	85	405	872	119

SW are ≈ 0.6 (Mullan and Smith, 2006), while in clouds β_p is typically around 0.1 (Lepping *et al.*, 2003). Also, they have lower turbulence levels and different turbulent properties (*e.g.*, Dasso, Gratton, and Farrugia, 2003; Matthaeus *et al.*, 2008).

MCs are a subset of ICMEs which are also characterized by abnormally low proton temperatures, bidirectional streaming of suprathermal electrons and energetic ions, enhanced helium abundance, strong magnetic fields with smooth field rotations, *etc.* (*e.g.*, Neugebauer and Goldstein, 1997, and references therein).

To study the distribution of correlation lengths in this transient component of the SW, we employ the defining criterion by Richardson and Cane (1995) and retain those intervals showing an observed temperature lower than one-half of the expected temperature for usual SW (Lopez and Freeman, 1986; Démoulin, 2009). Since the analysis of this transient component reduces significantly the amount of available data, we use only ACE data and broaden the range of F to ($5^{\rm th}$-$95^{\rm th}$) percentiles to increase the amount of intervals to be analyzed.

The non-linear least-square fit to the distribution of $\ln(\lambda)$ in this transient regime is shown in panel (b) of Figure 7 in dashdot line. The Gaussian fit is also normalized by the total area to facilitate comparison. The $\ln(\lambda)$ distribution for the transient regime is also wider than the high-$\beta_{\rm p}$ plasma samples and is even more displaced to the right when compared to the low-$\beta_{\rm p}$. JB test return a P$-$value equal to 0.29 giving good evidence favoring the hypothesis "correlation lengths in ICMEs follow a log-normal PDF". The last column in Table 2 shows the statistical parameters for this distribution.

Correlation lengths in ICMEs at 1 AU have a distribution similar to that of low-$\beta_{\rm p}$ plasma but with a greater mean (see Table 2).

8. Summary, Discussion, and Conclusions

The spatial scales associated with the correlation length [λ] are related to the breakpoint in the spectrum, which separates the inertial range from the injection (low-frequency) range associated with large-scale structures in the SW (*e.g.*, presence of velocity shear). During the expansion of the wind, this breakpoint moves to the lower-frequency part of the spectrum (Tu, Pu, and Wei, 1984; Bruno *et al.*, 2005).

In this work, we have analyzed *Helios* 1 and 2, ACE, and *Ulysses* magnetic observations, restricted to the Ecliptic plane for different heliocentric distances [D]. From these observations, we characterized the distributions of λ in the solar wind, in low and high proton β SW regimes, and in ICMEs at 1 AU. We quantitatively investigated the hypothesis that the PDF of λ is log-normal.

In particular, we fitted the two free parameters of a normal distribution to the observed PDF of $\ln(\lambda)$. Qualitatively and with respect to the fitted parameters, all of the samples appear to be reasonably well described by a log-normal distribution. Then we applied the Jarque-Bera goodness-of-fit test in order to quantify departures from log-normality of the PDFs. We find, in the case of H1+H2 and *Ulysses* data, clear evidence (*i.e.*, $Pv > \alpha = 0.05$) in favor of concluding that λ is log-normally distributed. On the other hand, evidence is not so conclusive regarding ACE data: such a low Pv indicates that we should reject the hypothesis.

We also studied the distribution of correlation lengths in low-$\beta_{\rm p}$ and high-$\beta_{\rm p}$ SW regimes and estimated moments of the distribution. In each case, moments of $\ln(\lambda)$ evolve towards what is expected for a Gaussian PDF. Evaluation of the hypothesis of a normal distribution for $\ln(\lambda)$ by means of the JB test yield $Pv > \alpha = 0.05$ in all cases. We conclude that the distribution of magnetic-correlation lengths can be regarded as log-normal when considering individually the low-$\beta_{\rm p}$

and high-$\beta_{\rm p}$ solar-wind regimes. Evidently the conclusion is now equally strong for all three spacecraft; the identification of a log-normal distribution in the ACE analysis is much more conclusive when the data was sorted by proton β.

Furthermore, the λ-distribution for the high-$\beta_{\rm p}$ plasma is narrower and displaced to the left with respect to the low-$\beta_{\rm p}$ case. While in the former regime the fluctuating amplitude is larger than in the latter, correlation lengths take smaller values in the former (high-$\beta_{\rm p}$ sample), contrary to what is expected from MHD turbulence theories such as the Kármán and Howarth HD approach (von Kármán and Howarth, 1938). We interpret this behavior of λ as a consequence of the different initial conditions of the magnetic-field fluctuations at the solar corona for the two kinds of solar wind, with the initial λ in high-$\beta_{\rm p}$ smaller than in the low-$\beta_{\rm p}$ SW.

Besides its stationary component, the SW has several transient components, of which ICMEs are an example. We separate this transient component (only at 1 AU) from the usual SW retaining intervals with an observed temperature lower than one-half of the expected temperature for usual SW (Richardson and Cane, 1995). The distribution of λ is similar to but displaced to the right with respect to the low-$\beta_{\rm p}$ case. The JB test yields in this case the largest Pv so the hypothesis of a log-normal PDF for λ can be again accepted.

The PDF of λ evolves with the distance to the Sun. For larger heliocentric distances we found a narrower distribution (a decreasing σ^2 with D), and nearer to a log-normal distribution of λ. From Table 1 is possible to see that for increasing heliocentric distance, the moments of the PDF of $\ln(\lambda)$ [γ, K, and M_6] tend progressively to those values expected for a normal distribution. This result is consistent with multiplicative processes involving λ occurring in the solar wind, and a consequent relaxation to a log-normal PDF. We confirmed that λ increases with the heliocentric distance [D] and with the nominal SW aging [$T = D/V_{SW}$], and found that $\lambda(D) = 0.89(D/1\,AU)^{0.43} \times 10^6\,\mathrm{km}$ and $\lambda(T) = 0.11(T/1\,\mathrm{hour})^{0.47} \times 10^6\,\mathrm{km}$, for the ranges [0.3 - 5.3]AU and [30 - 670] hours, respectively. We find this overall behavior also in the low-$\beta_{\rm p}$ and high-$\beta_{\rm p}$ regimes: λ grows with D and T in both cases.

In the near-Ecliptic structured solar wind, fluctuations of the magnetic field are present over a large range of spatial and temporal scales. These multiscale structures partially originate at the Sun and evolve due to the local turbulent dynamics in the solar wind. In this context we infer that near the Sun, before the Alfvénic critical point, λ follows a log-normal probability distribution function in both high-$\beta_{\rm p}$ and low-$\beta_{\rm p}$ solar wind, whose parameters continue to evolve due to the solar-wind turbulent dynamics. The distribution remains approximately log-normal, and evolves more precisely towards this form due to multiplicative processes in the turbulent solar wind.

Acknowledgements MER is a fellow from CONICET. SD is a member of the Carrera del Investigador Científico, CONICET. MER and SD acknowledge partial support by Argentinean grants UBACyT 20020120100220 (UBA) and PIP 11220090100825/10 (CONICET). WHM acknowledge partial support by NFS Shine AGS 1156094, Solar Terrestrial Program AGS 1063439, and the Solar Probe Plus ISIS Project. We thank E. Marsch for providing *Helios* data.

Appendix

A. Log-normal PDFs

A probability distribution function (PDF) of variable x is said to be log-normal if:

$$y = f_L(x|\mu,\sigma) = \frac{1}{x\sigma\sqrt{2\pi}} \exp\left[-\frac{(\ln(x)-\mu)^2}{2\sigma^2}\right] \tag{7}$$

The Gaussian (or normal) distribution and the log-normal distribution are related. Let Y be a random variable log-normally distributed with parameters μ and σ, then $x = \ln(Y)$ will be a random variable normally distributed with mean μ and standard deviation σ. The mean $[m]$, median $[m^*]$, and variance $[var]$ of Y are functions of the parameters μ and σ (Mood, Graybill, and Boes, 1974) given by:

$$m = \exp\left(\mu + \frac{\sigma^2}{2}\right), \quad m^* = \exp(\mu), \quad var = [\exp(\sigma^2) - 1]\exp(2\mu + \sigma^2) \tag{8}$$

and μ and σ are the mean and standard deviation of $x = \ln(Y)$ (normally distributed).

Log-normal forms are a possible fit when the distribution of a positive-definite random variable has a low mean, large variance, and is asymmetric with long tail to high values, larger than the mean value (Limpert, Stahel, and Abbt, 2001). Log-normal PDFs are usually encountered when the observable variable results from a large number of independent processes operating simultaneously. The long tail exhibits non-linear interactions and multiplicative processes, thus making the log-normal PDF suitable for the description of highly variable observations.

B. Goodness-of-fit Hypothesis Test and P−value

When fitting a statistical model to observed data, one may want to know how well the model actually reflects the observations. That is, how close are the observed values to those which would be expected under the fitted model? There are statistical hypothesis tests that addresses this issue.

Any hypothesis test uses a statistic ξ, namely a certain quantity calculated from the data whose probability distribution function $[f]$ is known, assuming that the hypothesis to be tested is true. In the particular case of the Jarque–Bera (Jarque and Bera, 1980) test, ξ_{JB} was already introduced in Equation (6): $\xi_{JB} = \frac{n}{6}\left(\gamma^2 + \frac{(K-3)^2}{4}\right)$. In order to accept or reject the hypothesis we need a decision rule. If the computed $\xi_{\rm obs}$ is larger than a critical value $\xi_{\rm critical}$ (chosen *a priori*), then the observed and expected values are not close enough and the model is a poor fit to the data.

One can state the decision rule in probabilistic terms. The probability of rejecting a true hypothesis is the significance α

$$\alpha = \int_{\xi_{critical}}^{\infty} f(\xi)\mathrm{d}\xi \tag{9}$$

Stated in this way, α determines the critical value $\xi_{\rm critical}$ of the statistic in use (Frodesen, Skjeggestad, and Tofte, 1979). Then, if after conducting the test, our ξ yields an observed value $\xi_{\rm obs}$ greater than $\xi_{\rm critical}$ (*i.e.* $\xi_{\rm obs} < \xi_{\rm critical}$), we should reject our hypothesis. Increasing α will increase the probability of incorrectly rejecting the hypothesis when it is true.

However, it is even more convenient to calculate the P-value Pv, defined, assuming the hypothesis to be true, as

$$Pv = \int_{\xi_{obs}}^{\infty} f(\xi)\mathrm{d}\xi \tag{10}$$

The P-value is the highest value of α that we can obtain from the test such that we do not reject the null hypothesis (Frodesen, Skjeggestad, and Tofte, 1979). Statistically speaking, the P-value is the probability of obtaining a result as extreme as, or more extreme than, the result actually obtained when the null hypothesis is true. The P-value (obtained for $\xi_{\rm obs}$) can be understood as follows: suppose that we perform another experiment which yields another observed value of the statistic $\xi^{'}_{\rm obs}$; then Pv is the probability that $\xi^{'}_{\rm obs}$ is greater than $\xi_{\rm obs}$ given that the null hypothesis is true. Namely, the P-value measures the strength of the evidence in support of a null hypothesis.

References

Altschuler, M.D., Trotter, D.E., Orrall, F.Q.: 1972, *Solar Phys.* **26**, 354. doi:doi.

Bale, S.D., Kasper, J.C., Howes, G.G., Quataert, E., Salem, C., Sundkvist, D.: 2009, *Physical Review Letters* **103**(21), 211101. doi:doi.

Batchelor, G.K.: 1953, *The theory of homogeneous turbulence*, Camb. Univ. Press, ???.

Bavassano, B., Dobrowolny, M., Mariani, F., Ness, N.F.: 1982, *J. Geophys. Res.* **87**, 3617. doi:doi.

Belcher, J.W., Davis, L. Jr.: 1971, *J. Geophys. Res.* **76**, 3534. doi:doi.

Bruno, R., Carbone, V.: 2013, *Living Reviews in Solar Physics* **10**, 2. doi:doi.

Bruno, R., Carbone, V., Bavassano, B., Sorriso-Valvo, L.: 2005, *Adv. Space Res.* **35**, 939. doi:doi.

Bruno, R., Carbone, V., Vörös, Z., D'Amicis, R., Bavassano, B., Cattaneo, M.B., Mura, A., Milillo, A., Orsini, S., Veltri, P., Sorriso-Valvo, L., Zhang, T., Biernat, H., Rucker, H., Baumjohann, W., Jankovičová, D., Kovács, P.: 2009, *Earth Moon and Planets* **104**, 101. doi:doi.

Burlaga, L.F., Lazarus, A.J.: 2000, *J. Geophys. Res.* **105**, 2357. doi:doi.

Burlaga, L.F., Ness, N.F.: 1998, *J. Geophys. Res.* **103**, 29719. doi:doi.

Campbell, W.H.: 1996, *J. Atmos. Terr. Phys.* **58**, 1171.

Coleman, P.J. Jr.: 1968, *Astrophys. J.* **153**, 371. doi:doi.

D'Amicis, R., Bruno, R., Pallocchia, G., Bavassano, B., Telloni, D., Carbone, V., Balogh, A.: 2010, *Astrophys. J.* **717**, 474. doi:doi.

Dasso, S., Gratton, F.T., Farrugia, C.J.: 2003, *J. Geophys. Res.* **108**, 1149. doi:doi.

Dasso, S., Milano, L.J., Matthaeus, W.H., Smith, C.W.: 2005a, *Astrophys. J.* **635**, L181. doi:doi.

Dasso, S., Mandrini, C.H., Démoulin, P., Luoni, M.L., Gulisano, A.M.: 2005b, *Adv. Space Res.* **35**, 711. doi:doi.

Démoulin, P.: 2009, *Solar Phys.* **257**, 169. doi:doi.

Démoulin, P., Dasso, S.: 2009, *Astron. Astrophys.* **498**, 551. doi:doi.

Frodesen, A.G., Skjeggestad, O., Tofte, H.: 1979, *Probability and statistics in particle physics*, Universitetsforl., Bergen, Norway.

Goldstein, M.L., Roberts, D.A., Matthaeus, W.H.: 1995, *Annual Rev. of Astron. Astrophys.* **33**, 283. doi:doi.

Gulisano, A.M., Démoulin, P., Dasso, S., Ruiz, M.E., Marsch, E.: 2010, *Astron. Astrophys.* **509**, A39. doi:doi.
Gulisano, A.M., Démoulin, P., Dasso, S., Rodriguez, L.: 2012, *Astron. Astrophys.* **543**, A107. doi:doi.
Horbury, T.S., Balogh, A., Forsyth, R.J., Smith, E.J.: 1995, *Geophys. Res. Lett.* **22**, 3401. doi:doi.
Horbury, T.S., Balogh, A., Forsyth, R.J., Smith, E.J.: 1996, *Astron. Astrophys.* **316**, 333.
Jarque, C.M., Bera, A.K.: 1980, *Economics Lett.* **6**(3), 255.
Klein, L.W., Matthaeus, W.H., Roberts, D.A., Goldstein, M.L.: 1992, In: Marsch, E., Schwenn, R. (eds.) *Solar Wind Seven Colloquium*, 197.
Lepping, R.P., Berdichevsky, D.B., Szabo, A., Arqueros, C., Lazarus, A.J.: 2003, *Solar Phys.* **212**, 425.
Limpert, E., Stahel, W.A., Abbt, M.: 2001, *BioScience* **51**(5), 341.
Lopez, R.E., Freeman, J.W.: 1986, *J. Geophys. Res.* **91**, 1701. doi:doi.
Mariani, F., Neubauer, F.M.: 1990, In: Schwenn, R., Marsch, E. (eds.) *The Interplanetary Magnetic Field*, 183.
Matthaeus, W.H., Goldstein, M.L.: 1982, *J. Geophys. Res.* **87**, 10347. doi:doi.
Matthaeus, W.H., Goldstein, M.L.: 1986, *Phys. Rev. Lett.* **57**, 495. doi:doi.
Matthaeus, W.H., Velli, M.: 2011, *Space Sci. Rev.* **160**, 145. doi:doi.
Matthaeus, W.H., Goldstein, M.L., Roberts, D.A.: 1990, *J. Geophys. Res.* **95**, 20673.
Matthaeus, W.H., Smith, C.W., Bieber, J.W.: 1999, In: Suess, S.T., Gary, G.A., Nerney, S.F. (eds.) *American Institute of Physics Conference Series*, *American Institute of Physics Conference Series* **471**, 511. doi:doi.
Matthaeus, W.H., Oughton, S., Pontius, D.H. Jr., Zhou, Y.: 1994, *J. Geophys. Res.* **99**, 19267. doi:doi.
Matthaeus, W.H., Dasso, S., Weygand, J.M., Milano, L.J., Smith, C.W., Kivelson, M.G.: 2005, *Phys. Rev. Lett.* **95**(23), 231101. doi:doi.
Matthaeus, W.H., Weygand, J.M., Chuychai, P., Dasso, S., Smith, C.W., Kivelson, M.G.: 2008, *Astrophys. J. Lett.* **678**, L141. doi:doi.
McComas, D.J., Elliott, H.A., Schwadron, N.A., Gosling, J.T., Skoug, R.M., Goldstein, B.E.: 2003, *Geophys. Res. Lett.* **30**, 1517. doi:doi.
Milano, L.J., Dasso, S., Matthaeus, W.H., Smith, C.W.: 2004, *Phys. Rev. Lett.* **93**(15), 155005. doi:doi.
Montroll, E.W., Shlesinger, M.F.: 1982, *Proceedings of the National Academy of Science* **79**, 3380. doi:doi.
Mood, A.M., Graybill, F.A., Boes, D.C.: 1974, *Introduction to the theory of statistics*, 3rd edn. McGraw-Hill, New York, USA.
Mullan, D.J., Smith, C.W.: 2006, *Solar Phys.* **234**, 325. doi:doi.
Neugebauer, M., Goldstein, R.: 1997, *Washington DC American Geophysical Union Geophysical Monograph Series* **99**, 245. doi:doi.
Oughton, S., Dmitruk, P., Matthaeus, W.H.: 2006, *Phys. Plasmas* **13**(4), 042306. doi:doi.
Padhye, N.S., Smith, C.W., Matthaeus, W.H.: 2001, *J. Geophys. Res.* **106**, 18635. doi:doi.
Richardson, I.G., Cane, H.V.: 1995, *J. Geophys. Res.* **100**, 23397. doi:doi.
Ruiz, M.E., Dasso, S., Matthaeus, W.H., Marsch, E., Weygand, J.M.: 2011, *J. Geophys. Res.* **116**, 10102. doi:doi.
Smith, C.W., Matthaeus, W.H., Zank, G.P., Ness, N.F., Oughton, S., Richardson, J.D.: 2001, *J. Geophys. Res.* **106**, 8253. doi:doi.
Taylor, G.I.: 1938, In: *Proc. R. Soc. London Ser. A* **164**, 476.
Thadewald, T., Büning, H.: 2007, *J. Appl. Stat.* **34**(1), 87.
Tu, C.-Y., Marsch, E.: 1995, *MHD structures, waves and turbulence in the solar wind: observations and theories*, Kluwer, Belgium.
Tu, C.-Y., Pu, Z.-Y., Wei, F.-S.: 1984, *J. Geophys. Res.* **89**, 9695. doi:doi.
von Kármán, T., Howarth, L.: 1938, *Proc. R. Soc. London Ser. A* **164**, 192. doi:doi.
Wicks, R.T., Owens, M.J., Horbury, T.S.: 2010, *Solar Phys.* **262**, 191.